

# Constraints on asteroid-mass primordial black holes in dwarf galaxies using Hubble Space Telescope photometry

Nicolas Esser<sup>1,\*</sup>, Carrie Filion<sup>2</sup>, Sven De Rijcke<sup>3</sup>, Nitya Kallivayalil<sup>5</sup>, Hannah Richstein<sup>5</sup>, Peter Tinyakov<sup>1</sup>, and Rosemary F.G. Wyse<sup>4</sup>

<sup>1</sup> Service de Physique Théorique, Université Libre de Bruxelles, Boulevard du Triomphe, CP225, 1050 Brussels, Belgium

<sup>2</sup> Center for Computational Astrophysics, Flatiron Institute, 162 Fifth Ave, New York, NY 10010, USA

<sup>3</sup> Department of Physics and Astronomy, Ghent University, Krijgslaan 281, 9000 Ghent, Belgium

<sup>4</sup> Department of Physics & Astronomy, The Johns Hopkins University, Baltimore, MD 21218, USA

<sup>5</sup> Department of Astronomy, The University of Virginia, 530 McCormick Road, Charlottesville, VA 22904, USA

March 6, 2025

## ABSTRACT

Primordial black holes (PBHs) in the asteroid-mass range remain a viable and until now unconstrained dark matter (DM) candidate. If such PBHs exist, they could be captured by stars in DM-dominated environments with low velocity dispersion such as ultra-faint dwarf galaxies (UFDs). The capture probability increases with the stellar mass, and captured PBHs would rapidly destroy their host stars. As a result, the presence of PBHs in UFDs would alter their stellar mass functions. Using photometric observations of three ultra-faint dwarf galaxies from the Hubble Space Telescope, we show that it is unlikely that their mass functions have been significantly modified by PBHs, and we place constraints on the PBH abundance. In the ultra-faint dwarf galaxy Triangulum II, PBHs around  $10^{19}$  g are excluded at the  $2\sigma$  ( $3\sigma$ ) level from constituting more than  $\sim 55\%$  ( $\sim 78\%$ ) of the dark matter, while the possibility that PBHs represent the entirety of the DM is excluded at the  $3.7\sigma$  level.

**Key words.** Methods: statistical – techniques: photometric – stars: luminosity function, mass function – galaxies: dwarf – galaxies: stellar content – dark matter

## 1. Introduction

Primordial black holes (PBHs) are theoretical objects that may have formed during the early stages of the Universe. First proposed more than 50 years ago by Zel'dovich & Novikov (1967) and Hawking (1971), these black holes can have any mass, and may offer an explanation for dark matter (DM). However, many constraints have been placed on their abundance – typically expressed as the PBH fraction relative to the total dark matter  $f_{\text{PBH}} = \Omega_{\text{PBH}}/\Omega_{\text{DM}}$  – across different mass ranges (Carr et al. 2021). Presently, only one mass range remains viable for PBHs to constitute all the dark matter, specifically the "asteroid-mass" range, which spans approximately from  $10^{17}$  to  $10^{23}$  g. Black holes within this range are microscopic in size but sufficiently massive to evade Hawking radiation, making them particularly challenging to probe.

In this work, we assess the viability of asteroid-mass PBHs as a dark matter candidate. We explore the scenario in which stars capture PBHs during their formation (Esser & Tinyakov 2023; Oncins et al. 2022). A star "infected" by a PBH would undergo rapid accretion, leading to the star's destruction and the formation of a subsolar-mass black hole. The impact of this destruction process on stellar populations is expected to be significant in dark-matter-dominated environments with low velocity dispersion, where the probability of destruction approaches unity, as in some ultra-faint dwarf galaxies (UFDs).

UFDs are low luminosity, low surface-brightness systems that host old, metal-poor stellar populations. Along with the Galactic

centre, they are the systems with the highest inferred dark-matter density. Due to their faintness, even the most massive UFDs orbiting the Milky Way were only recently detected and identified (see, e.g., Belokurov et al. 2007 and the review by Simon 2019).

Esser et al. (2024) showed that the likelihood of PBH capture by stars depends on the stellar mass, with more massive stars having a higher probability of capturing PBHs and consequently being destroyed. Thus, the presence of primordial black holes should modify the stellar mass functions of their host galaxies. If the dark matter in UFDs were composed of asteroid-mass PBHs, a depletion of more massive stars in these galaxies would be expected, leading to a bottom-heavy mass function compared to the case of non-PBH dark matter. In Esser et al. (2024), the sensitivity of the mass function to this effect was investigated using synthetic data. It was shown that, in the absence of PBH-induced depletion, the statistics of the existing data could already provide constraints on the PBH fraction in dark matter,  $f_{\text{PBH}}$ , to below 100%.

In this paper, we analyse ultra-deep photometric observations of stars in three local UFDs — Reticulum II, Segue 1, and Triangulum II — conducted with the Hubble Space Telescope's (HST) Advanced Camera for Surveys (ACS). By fitting the data with standard models for the stellar mass function, modified to account for the star destruction process by PBHs, we constrain the abundance of primordial black holes in these galaxies. More specifically, we employ a "control sample" strategy exploiting the fact that, although the three galaxies in our sample share similar characteristics, the impact of PBHs on the stellar mass function of Reticulum II is expected to be negligible even when  $f_{\text{PBH}} = 1$ , in contrast to the other two galaxies (see Sec. 3.1). Consequently,

\* nicolas.esser@ulb.be

we use the parameters inferred from Reticulum II to construct priors for the remaining UFDs, which we then use to derive constraints on the PBH abundance. With this approach we exclude, at  $3.7\sigma$  confidence level, PBHs with masses around  $\sim 10^{19}$ g as constituting the entirety of the dark matter.

The rest of this paper is organized as follows. In Sec. 2 we review the impact of primordial black holes on the stellar mass function. In Sec. 3 the relevant information and photometric data for our sample of galaxies is gathered. Sec. 4 describes the Bayesian procedure used to analyse the data given our mass function model. In Sec. 5 we show the results of the analysis and the constraints they imply for  $f_{\text{PBH}}$ . Sec. 6 contains concluding remarks.

## 2. Impact of PBHs on the stellar mass function

### 2.1. Initial mass function

Ultra-faint dwarf galaxies are old and relatively simple systems whose stars formed in only a short period of star formation around  $\sim 13$  Gyr ago (Sacchi et al. 2021), which resulted in a population of metal-poor stars with a very narrow spread of ages. Of this population, only stars with masses  $M \lesssim 0.8M_{\odot}$  presently remain on the main sequence, while heavier stars have either entered the giant branch or have already turned into compact objects. For stars below this mass, the present-day stellar mass function is thus, in the absence of the PBH destruction effect, essentially the same as the mass function of stars at birth, i.e., the initial mass function (IMF).

As a key topic in stellar astrophysics, the IMF has been extensively studied over the past few decades (see e.g. the review of Bastian et al. 2010). Two common fitting functions used to describe the IMF are the broken power-law (BPL), and the log-normal (LN) distribution. The broken power-law is parameterized as follows,

$$\frac{dN_i}{dM}(M, \alpha_1, \alpha_2) \propto \begin{cases} M^{\alpha_1} & \text{for } 0.08M_{\odot} \leq M < 0.5M_{\odot} \\ kM^{\alpha_2} & \text{for } M \geq 0.5M_{\odot}, \end{cases} \quad (1)$$

with the continuity constant  $k = (0.5M_{\odot})^{(\alpha_1 - \alpha_2)}$  and  $\alpha_{1,2}$  the two power-law exponents. For  $\alpha_1 = -1.3$  and  $\alpha_2 = -2.3$ , the standard Kroupa (2001) IMF is recovered. The log-normal distribution is given by

$$\frac{dN_i}{dM}(M, M_c, \sigma_{\text{LN}}) \propto \frac{1}{M} \exp\left(-\frac{[\log_{10}(M/M_c)]^2}{2\sigma_{\text{LN}}^2}\right), \quad (2)$$

where  $M_c$  is the characteristic mass and  $\sigma_{\text{LN}}$  is the width of the distribution. The single-star Chabrier (2003) IMF is recovered for  $M_c = 0.08M_{\odot}$  and  $\sigma_{\text{LN}} = 0.69$ .

### 2.2. Star destruction by PBHs

When a protostellar cloud contracts to form a star, it drags along the surrounding dark matter, creating a DM overdensity around the newly formed star. If the dark matter consists of asteroid-mass PBHs, this process results in an enhanced density of PBHs orbiting the star. Some of these PBHs may follow orbits that pass through the star. During each passage, these PBHs lose energy due to dynamical friction and accretion of stellar material, causing their orbits to gradually shrink. After sufficient encounters, their orbits become entirely confined within the star. At this stage, the accretion of stellar material becomes significantly more efficient, so that, assuming Bondi (1952) accretion regime, the star gets destroyed in a time (much) shorter than  $\sim 10$  Gyr.

This process, first applied to the case of neutron stars and white dwarfs (Capela et al. 2013, 2014), was studied by Esser & Tinyakov (2023) and Oncins et al. (2022) in the context of main-sequence stars. It was subsequently shown that the probability that a star captures a PBH increases with the star’s mass. Consequently, more massive stars are more prone to destruction by PBHs, influencing the stellar mass function.

We follow the formalism of Esser et al. (2024) to model the effect of primordial black holes on the stellar population in the mass range  $[10^{19}, 10^{21}]$ g. The capture of PBH by a star is a random process that can be characterized by the mean number  $\bar{N}$  of PBHs captured over a star’s lifetime (13 Gyr for stars in UFDs). This quantity is proportional to the PBH fraction in DM,  $f_{\text{PBH}}$ , and to the local DM density,  $\rho_{\text{DM}}$ , and inversely proportional to the cube of the PBH 3d velocity dispersion<sup>1</sup>,  $\sigma_v$ . Therefore, it can be written as

$$\bar{N} = f_{\text{PBH}} \eta \nu(M), \quad (3)$$

where the “merit factor”

$$\eta = \frac{\rho_{\text{DM}}}{100 \text{ GeV/cm}^3} \left(\frac{7 \text{ km/s}}{\sqrt{2}\sigma_v}\right)^3 \quad (4)$$

reflects the specific conditions in a given UFD. The function  $\nu(M)$  represents the mean number of PBHs captured under reference conditions:  $f_{\text{PBH}} = 1$ ,  $\rho_{\text{DM}} = 100 \text{ GeV/cm}^3$  and  $\sigma_v = 7 \text{ km/s}$ , by a star at rest. The factor  $\sqrt{2}$  accounts for the motion of stars relative to the DM halo. The function  $\nu(M)$  has been calculated numerically in Esser et al. (2024). For practical use, an approximation valid in the stellar mass range  $[0.2, 0.8]M_{\odot}$  is given by

$$\nu(M) = a(M/M_{\odot})^b + c, \quad (5)$$

with  $a = 3.76$ ,  $b = 0.685$  and  $c = -0.883$ .

According to Poisson statistics, stars have a likelihood

$$P_S(M, f_{\text{PBH}}) = \exp(-\bar{N}) = \exp[-f_{\text{PBH}}\eta\nu(M)] \quad (6)$$

of avoiding destruction by PBHs. Note that this survival probability depends exponentially on  $\eta$ . Moreover, the dependence on  $\eta$  is degenerate with that on  $f_{\text{PBH}}$ . Examples of the function  $P_S$  are displayed on Fig. 1.

Approximating the stellar population as single-age, the present-day stellar mass function combines the initial mass function with the effect of PBHs, and is given by

$$\frac{dN}{dM}(M, \theta, f_{\text{PBH}}) \propto \frac{dN_i(M, \theta)}{dM} \times P_S(M, f_{\text{PBH}}), \quad (7)$$

where  $\theta$  stands for the IMF parameters, i.e.  $\{\alpha_1, \alpha_2\}$  for the BPL and  $\{M_c, \sigma_{\text{LN}}\}$  for the LN distribution. This mass function will serve as a model that we will fit to real data in Sec. 4.

### 2.3. PBHs and binary stars

The formalism presented in Esser et al. (2024) applies to isolated stars. However, a significant fraction of stars are in binary systems, so it is essential to evaluate the impact of companion stars on the PBH capture probability. Three-body interactions, which

<sup>1</sup> Throughout this paper we assume the same isotropic velocity distribution for both DM and stars, and use  $\sigma_v$  to denote the 3d velocity dispersion, which is related to the measured line-of-sight velocity dispersion by  $\sigma_{\text{los}} = \sigma_v / \sqrt{3}$ .

involve the primary star, its companion, and a PBH, could alter the trajectories of PBHs around the primary star. These interactions might cause some PBHs to be ejected from star-crossing orbits, while others could be drawn into such orbits. The net effect of companion stars is therefore not obvious and has not yet been quantified.

In the absence of a complete solution to the problem, the simplest approach is to disregard PBH capture in binary systems altogether. However, this assumption is overly conservative. The significant uncertainties in the binary fraction within UFDs ultimately prevent meaningful constraints from being placed on the PBH abundance. To make further progress, a more detailed investigation of the PBH capture process is required. As we show in Appendix A, for smaller PBH masses, the capture probability is dominated by PBHs with initially tighter orbits, which are less affected by perturbations from a companion star. Consequently, the effect of the companion star can be ignored, and Eq. (5) remains valid as is, for PBH masses around  $10^{19}$ g.

### 3. Ultra-faint dwarf galaxy sample

The initial mass function has been studied in detail by Filion et al. (2022) and Filion et al. (2024) in five UFDs: Reticulum II, Segue 1, Triangulum II, Ursa Major II, and Boötes I. Among these, the first three are similar in age, metallicity, and velocity dispersion, making them a good sample for our study. Relevant information about these galaxies, along with the photometric data used in this analysis, is provided in the following subsections.

#### 3.1. The merit factors

The merit factors  $\eta$  of the UFDs are inferred from the measured quantities compiled by Simon (2019). We first estimate the total mass of a given UFD, based on its measured projected half-light radius  $R_{1/2}$  and line-of-sight velocity dispersion  $\sigma_{\text{los}}$ , which we plug into the half-light mass estimator from Wolf et al. (2010). The DM density is obtained by dividing the half-light mass by the half-light volume, which is taken as the volume of the sphere of deprojected half-light radius given by  $r_{1/2} = 4R_{1/2}/3$  (Simon 2019). We assume that DM dominates the mass of the UFD. The merit factor can then be computed according to Eq. (4). The relevant information and the resulting merit factors are compiled in Table 1.

	Ret. II	Seg. 1	Tri. II	Refs.
$R_{1/2}$ [pc]	51	24	16	[1]
$\sigma_v$ [km/s]	5.7	6.4	< 5.9	[2,3,4]
$\rho_{\text{DM}}$ [GeV/cm <sup>3</sup> ]	15	85	161	/
$\eta$	<b>0.097</b>	<b>0.39</b>	<b>0.95</b>	/

Table 1: The dynamical properties of dwarf galaxies used throughout this work. Where only an upper limit on  $\sigma_{\text{los}}$  is available, we conservatively use this limit as a value of  $\sigma_{\text{los}}$ . Refs: [1] Muñoz et al. (2018), [2] Simon et al. (2015), [3] Kirby et al. (2017), [4] Simon et al. (2011).

We also considered the case where the DM is not uniformly distributed but follows a cuspy NFW profile (Navarro et al. 1997) and the stars a cored profile (Plummer 1911) within the UFD. We found that it typically results in a mild  $O(10\%)$  enhancement in the average star destruction probability, dependent on the stellar

mass. A more detailed investigation of non-uniform dark matter and stellar distributions is left for future work.

In Fig. 1, we show the probability of stars surviving from destruction by PBHs (Eq. (6)) in the three galaxies of our sample, assuming that PBHs constitute all the DM. One can see from this plot that, for  $f_{\text{PBH}} = 1$ , the star-destruction effect of PBHs is negligible in Reticulum II ( $\eta = 0.097$ ), moderate in Segue 1 ( $\eta = 0.39$ ), and strong in Triangulum II ( $\eta = 0.95$ ). According to this observation, we use the galaxies Segue 1 and Triangulum II to test the PBH abundance, while Reticulum II will be used as a “control sample” as explained in detail in Sec. 5.

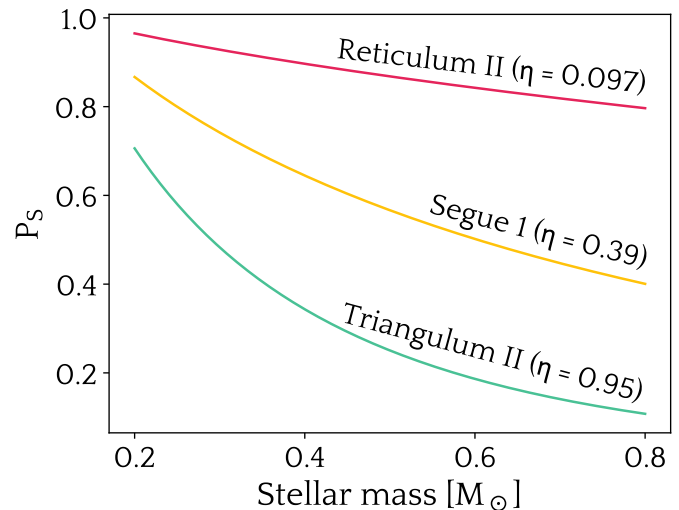


Fig. 1: Probability  $P_S$ , as a function of the stellar mass, of stars surviving from destruction by PBHs in three UFD galaxies: Reticulum II (upper curve), Segue 1 (middle curve) and Triangulum II (lower curve), assuming  $f_{\text{PBH}} = 1$ .

#### 3.2. HST photometric observations

We use photometric observations of the central regions of the UFD galaxies Reticulum II, Segue 1, and Triangulum II from the Hubble Space Telescope Advanced Camera for Surveys (HST-ACS) Treasury Program GO-14734 (PI: N. Kallivayalil). Here, we summarize some relevant details of the data processing. A more in-depth description can be found in Filion et al. (2024) and Richstein et al. (2024).

The imaging data for each galaxy were taken in the F814W and F606W filters of the ACS instrument with the Wide Field Channel. The exposures were then processed to only retain the starlike sources, removing most of the other light sources, which can be attributed to contaminants such as background galaxies or cosmic rays. Note that these remaining sources may not only be single stars, but may also be unresolved binary systems. Among the remaining sources in the field, one needs to identify the stars which are members of the targeted galaxy. To do this, we rely on the use of the Dartmouth Stellar Evolution Database (Dotter et al. 2008), which provides isochrone models for the position of stars of various masses on the colour-magnitude diagram (CMD) for a given age and metallicity.

We generate a solar-scaled isochrone, i.e. with solar ratios of all chemical elements other than iron, for a 13 Gyr old stellar population with a metallicity of  $[\text{Fe}/\text{H}] = -2.5$ , the lowest metallicity available in the Dartmouth Database and the closest to the mean metallicities measured in these galaxies (cf. Table 2

in Filion et al. 2024). We then convert this isochrone, originally in absolute magnitude, to apparent magnitude by correcting for the distance and reddening, based on the data from Table 1 of Filion et al. (2024). For the latter, we use the Spanish Virtual Observatory (SVO) filter-profile service<sup>2</sup> to convert the V-band extinction values  $A_V$  into extinction values for the F814W and F606W pass bands. The shifted isochrone is depicted in yellow on the CMD in Fig. 2.

Real sources deviate from this theoretical model due to various effects, and are consequently spread around the isochrone curve. Following Filion et al. (2024), we therefore consider as likely member stars the sources that are bluer than the isochrone by less than 0.3 mag in colour (left side of the isochrone) or redder by less than 0.4 mag (right side of the isochrone). The larger value on the red side is chosen to account for unresolved binary stars, which generate points that are redder than single stars with the same luminosity.

Furthermore, the effect of data completeness must be taken into account. Richstein et al. (2024) performed artificial star tests to estimate the 50% completeness limits of the UFD observations used in this work. To minimize uncertainties in star counts, we restrict the likely member sources to those with magnitudes below (i.e., brighter than) these limits, denoted by  $F814W_{\max}$  and  $F606W_{\max}$ . Additionally, we restrict the likely members sample to stars that are expected to still be on the main sequence, according to the Dartmouth model, which corresponds to selecting stars with magnitudes above  $F814W_{\min}$ . The values of these limits can be found in the Table 1 of Filion et al. (2024).

We end up with samples containing 1108, 559 and 608 likely members sources for Reticulum II, Segue 1 and Triangulum II respectively<sup>3</sup>. As an example, we display on Fig. 2 the colour-magnitude diagram of all the star-like sources of Reticulum II, alongside the theoretical isochrone model that is used to identify the likely members stars that lie within the coloured region on the plot. The CMDs of the other two galaxies can be found in Appendix B. The resulting catalogues of likely members will be used in the following section to study the stellar mass function and the possible presence of asteroid-mass PBHs in these galaxies.

## 4. Bayesian inference procedure

### 4.1. Synthetic stellar populations

The observational data takes the form of colour-magnitude diagrams, with each source (which can be either a single star or an unresolved binary system) providing a magnitude value in both the F606W and F814W pass bands. However, the model present-day mass function from Sec. 2 describes the distribution of stars as a function of their masses, not their magnitudes. Unfortunately, it is impossible to accurately recover stellar masses from the observed magnitudes, as one would need to know the metallicity of each individual star, identify which sources are in fact unresolved binaries, and know what is the photometric error associated with each measured magnitude. Instead, we use the “forward modelling” strategy, as described in Filion et al. (2022), which allows us to compare the real observed magnitude values with synthetic ones constructed from a model IMF.

To produce these mock observations, we first generate masses according to the present-day mass function as given in Eq. (7) above. Note that this mass function takes into account the effect of PBHs, and depends on 3 parameters – the two IMF parameters

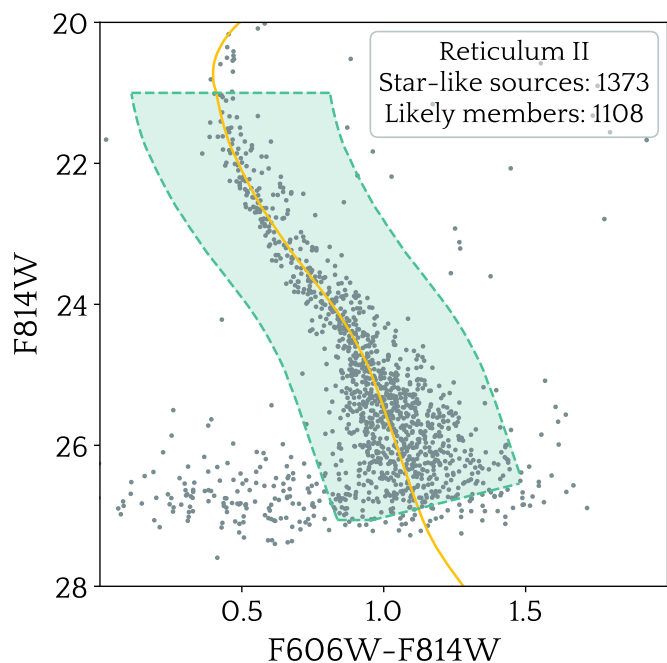


Fig. 2: Colour-magnitude diagram of Reticulum II. The solid line represents the Dartmouth isochrone for a population of 13 Gyr old stars with metallicity  $[Fe/H] = -2.5$ , corrected for distance and extinction. The points correspond to the observed star-like sources, while the coloured region encompasses the stars that are likely members of the galaxy and that will be used to study its stellar mass function.

represented by  $\theta$  of Sec. 2.1, and the PBH fraction  $f_{PBH}$ . We also fix the binary fraction<sup>4</sup>  $f_b$  and randomly pair some of these masses together. We then draw a metallicity for each star from a truncated Gaussian distribution with mean, dispersion, and truncation points specified by the values in Table 2 of Filion et al. (2024). We make sure that both stars in a given binary system are assigned the same metallicity.

Using isochrone curves from the Dartmouth Stellar Evolution Database (Dotter et al. 2008), each mass and metallicity combination is converted into absolute F814W and F606W magnitudes by interpolating the solar-scaled 13 Gyr old isochrones. Note that for stars that were attributed a metallicity  $[Fe/H] < -2.5$ , we use the isochrone with the lowest available metallicity, i.e.  $[Fe/H] = -2.5$ . The total magnitude of a binary is obtained by summing the fluxes of both stars. Based on the distance and reddening measurements in Table 1 of Filion et al. (2024), we then convert the absolute magnitudes into apparent magnitudes. We model the uncertainties on these parameters by adding a random Gaussian error, identical for all stars of a given population realization, with a width of 20% on  $A_V$  and 1 kpc on the distance before converting the magnitudes. We also model the effects of photometric errors by generating a Gaussian noise for each source. The mean of this Gaussian noise is 0, and its dispersion is obtained by fitting the magnitude-dependent errors measured in both bands for the real

<sup>4</sup> In this work, the binary fraction  $f_b$  is defined as the ratio of the number of actual stars which are members of binary systems to the total number of stars. However, another convention has sometimes been used in previous IMF analyses (e.g., Geha et al. 2013), with the binary fraction  $f_g$  being defined as the fraction of sources in the sky that are, in fact, binaries and not single stars. This definition can be recovered using  $f_g = f_b / (2 - f_b)$ .

<sup>2</sup> Available at <http://svo2.cab.inta-csic.es/theory/fps/>.

<sup>3</sup> The difference between these numbers and those in Filion et al. (2024) is due to roundings and update of the values on the SVO website.

data. Finally, to model the incompleteness of the real data, we apply rejection sampling to remove some stars using the completeness values derived in Richstein et al. (2024) and following the functional form described in Appendix C2 of El-Badry et al. (2017). We also apply the same magnitude cuts as those used for the real data.

While stars were initially generated with masses in the range  $[0.1, 1]M_{\odot}$ , the application of magnitude cuts restricts the low-mass end to approximately the completeness limit and the high-mass end to  $\lesssim 0.8M_{\odot}$ . However, low-mass stars ( $\lesssim 0.15M_{\odot}$ ) could still avoid the magnitude cuts and remain in the sample, provided they are members of binary systems. The expression (5), originally derived for stars with masses  $\in [0.2, 0.8]M_{\odot}$ , is therefore extrapolated to masses between 0.1 and  $0.2M_{\odot}$ . It is also worth noting that the input binary fraction  $f_b$  may differ slightly from the final fraction observed in the mock dataset, as single and binary stars do not share the same magnitude distribution and thus have different probabilities of being excluded by the magnitude cuts.

Thus, the generated synthetic stellar populations depend on four parameters: the two IMF parameters  $\theta$ , the binary fraction  $f_b$  and the fraction of PBHs  $f_{\text{PBH}}$ . We make sure that the mock datasets contain the same number of sources than the real observations which they are supposed to mimic. One can then create a CMD, similar to the one in Fig. 2, but for the mock datasets. An example is displayed on Fig. 3.

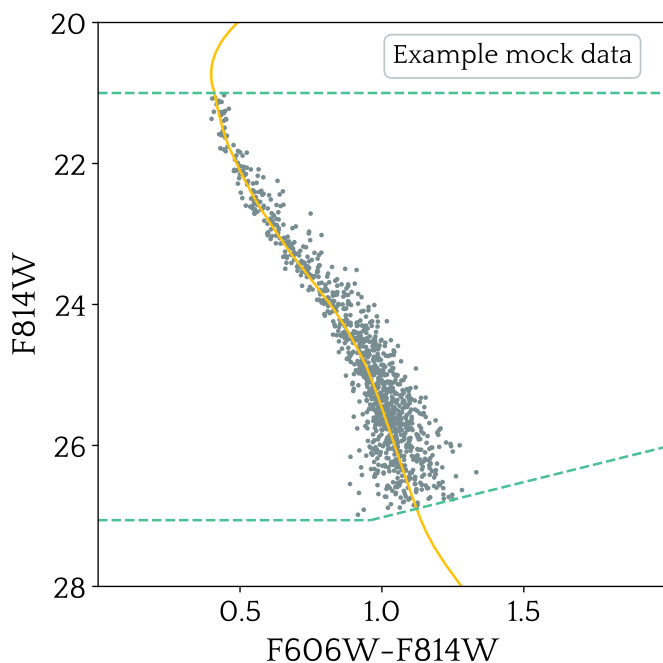


Fig. 3: Colour-magnitude diagram of a mock dataset. The solid line represents the Dartmouth isochrone for a population of 13 Gyr old stars with metallicity  $[\text{Fe}/\text{H}] = -2.5$ , corrected for distance and extinction. The points correspond to the generated star-like sources. This mock population was generated with the magnitude cuts (as shown by dashed lines) and physical parameters of Reticulum II, a Kroupa IMF, a binary fraction of 0.5 and assuming no PBH effect ( $f_{\text{PBH}} = 0$ ).

## 4.2. Approximate Bayesian Computation

To compare the real CMD of a given galaxy (Fig. 2) with the synthetic CMDs like the one shown in Fig. 3, we divide the unbinned CMDs into square bins of the size 0.2 mag. Both the observed and synthetic datasets are then represented as a list of  $\mathcal{O}(100)$  values of (normalized) source counts within bins. We choose the Jensen-Shannon distance between the mock and real lists as our distance metric. It was checked in Filion et al. (2022) and Filion et al. (2024) that the usage of other bin sizes or distance metric had no major impact on the results.

With this setup we obtain, for each realization of the mock dataset with given input parameters  $\{\theta, f_b, f_{\text{PBH}}\}$ , a number – the Jensen-Shannon distance – indicating how close this mock dataset is to the real data. Because of the many random variables involved in the generation of mock datasets, this number fluctuates even at fixed model parameters. This same randomness, coupled with the non-trivial relation between the stellar mass/metallicity and the magnitude, makes the task of defining a likelihood function for the model populations in magnitude space difficult. We thus perform a likelihood-free Approximate Bayesian Computation (ABC), which aims to find the model parameters that minimize the average distance between a large sample of mock datasets and the real data.

The workflow of the ABC using a Sequential Monte Carlo scheme (ABCSMC) as implemented within pyABC (Schälte et al. 2022) is the following. We choose a prior for each parameter (see Sec. 5) and sample from these priors, generating  $\mathcal{N} = 1000$  parameter values and corresponding star populations as described in Sec. 4.1. For each of them we calculate the associated Jensen-Shannon distance to the real data, thus getting an ensemble of “particles” where each particle represents a point in the parameter space and its associated distance to the data. The 90% quantile of smallest distances defines the acceptance threshold; particles above the threshold (10% of the original number) are discarded. The remaining set is used to generate a new ensemble of  $\mathcal{N}$  particles via importance sampling method, from which point the next iteration starts. We assume that the algorithm has reached convergence once three subsequent iterations have threshold values differing by less than 0.5%. We then run five additional steps, followed by one final step with an ensemble of  $10 \times \mathcal{N}$  particles, whose distribution in the parameter space is the posterior distribution we are looking for. In the analysis of Triangulum II (see Sec. 5.2), we instead used  $250 \times \mathcal{N}$  particles in the final step.

To ensure that the algorithm works properly, we generated several synthetic datasets and treated them as real data, aiming to recover the input parameters using the ABCSMC scheme. We tested populations ranging from 500 to 3000 stars, with various binary fractions, both the BPL and LN stellar mass function forms, and scenarios with and without the PBH effect. In all the tests the parameters  $\{\theta, f_b, f_{\text{PBH}}\}$  used to generate the synthetic data were consistently recovered within their statistical uncertainties.

## 5. Results and constraints on PBHs

### 5.1. Reticulum II: the control galaxy

We first turn to Reticulum II, a galaxy with low merit factor for which the effect of PBHs is expected to be negligible. Therefore, the present-day stellar mass function of this galaxy should be approximately equal to its initial mass function. We performed the ABCSMC analysis described in Sec. 4 for the two IMF parameters, the binary fraction, and the PBH fraction, with uniform



priors  $\alpha_{1,2} \in [-4.5, -0.05]$ ,  $M_c \in [0.05, 1]$ ,  $\sigma_{\text{LN}} \in [0.25, 1]$ ,  $f_b \in [0, 1]$  and  $f_{\text{PBH}} \in [0, 3]$ . These ranges cover a broad spectrum around the typical values of these parameters reported in previous studies.

The posterior distributions of the IMF parameters for both the BPL and the LN mass functions are shown in Fig. 4. The posterior distribution of  $f_{\text{PBH}}$  was found to be roughly uniform across its allowed range and is not displayed on the plot. This is the expected behaviour for this parameter since it does not influence the model due to the low merit factor of Reticulum II. We also verified that performing the ABCSMC analysis with fixed  $f_{\text{PBH}} = 0$  yielded the same posterior distributions for the other parameters, thus confirming that the PBH impact on Reticulum II is negligible.

These results are consistent within  $1\sigma$  with those obtained by Filion et al. (2024), with slightly tighter posteriors. One can see from these plots that the most constrained parameters are the low-mass slope for the BPL and the characteristic mass  $M_c$  for the LN initial mass function. This can be attributed to the fact that most stars in the samples have low masses, providing more data points to constrain these parameters, which are predominantly influenced by the low-mass data.

Another notable observation is the near absence of correlation between the IMF parameters and the binary fraction. While the IMF parameters primarily determine the distribution of points in luminosity (i.e. along the vertical axis of the CMD), the binary fraction influences how spread the data points are in colour (i.e. along the horizontal axis of the CMD), as binary stars appear redder than single stars with the same total luminosity.

Finally, note that modifying the isochrone model, the extinction, or the distance of the galaxy mainly results in theoretical curves that are shifted along the horizontal axis relative to those used here. We thus expect that among model parameters the binary fraction is most sensitive to the stellar population modelling. The other parameters should be fairly robust against systematic errors arising from the choice of isochrone. This concerns equally the PBH fraction whose main effect on the CMD is also along the vertical axis.

## 5.2. Segue 1 and Triangulum II: the test galaxies

In the analysis of Reticulum II in Sec. 5.1 we used broad uniform priors for all parameters. But, in general, there is no compelling reason to favour a flat prior over another function. Previous mass function analyses have explored other possibilities, such as a logarithmic prior (Gennaro et al. 2018).

For the particular question we address in this paper, however, there is a well-motivated choice. The three galaxies in our sample share several key properties: they have comparable ages, metallicities, and velocity dispersions, differing primarily in their inferred dark matter densities (see Table 1). While Reticulum II has multiple r-process enriched stars (Ji et al. 2016), and is likely a satellite of the Large Magellanic Cloud (Patel et al. 2020) whereas the other two UFDs are Milky Way satellites, all three galaxies also share comparable star formation histories (Sacchi et al. 2021; Simon et al. 2023). There is thus no reason to expect substantial variations in the mass function among these three systems. This assumption can be tested by applying the analysis of Sec. 5.1, with  $f_{\text{PBH}} = 0$ , to the other two galaxies. The results are presented in Appendix C. The inferred values of the IMF parameters are consistent within their statistical uncertainties among the three galaxies.

In contrast to other parameters, the merit factors (and, consequently, the expected effect of PBHs) in these galaxies differ significantly, being negligible in Reticulum II and substantial

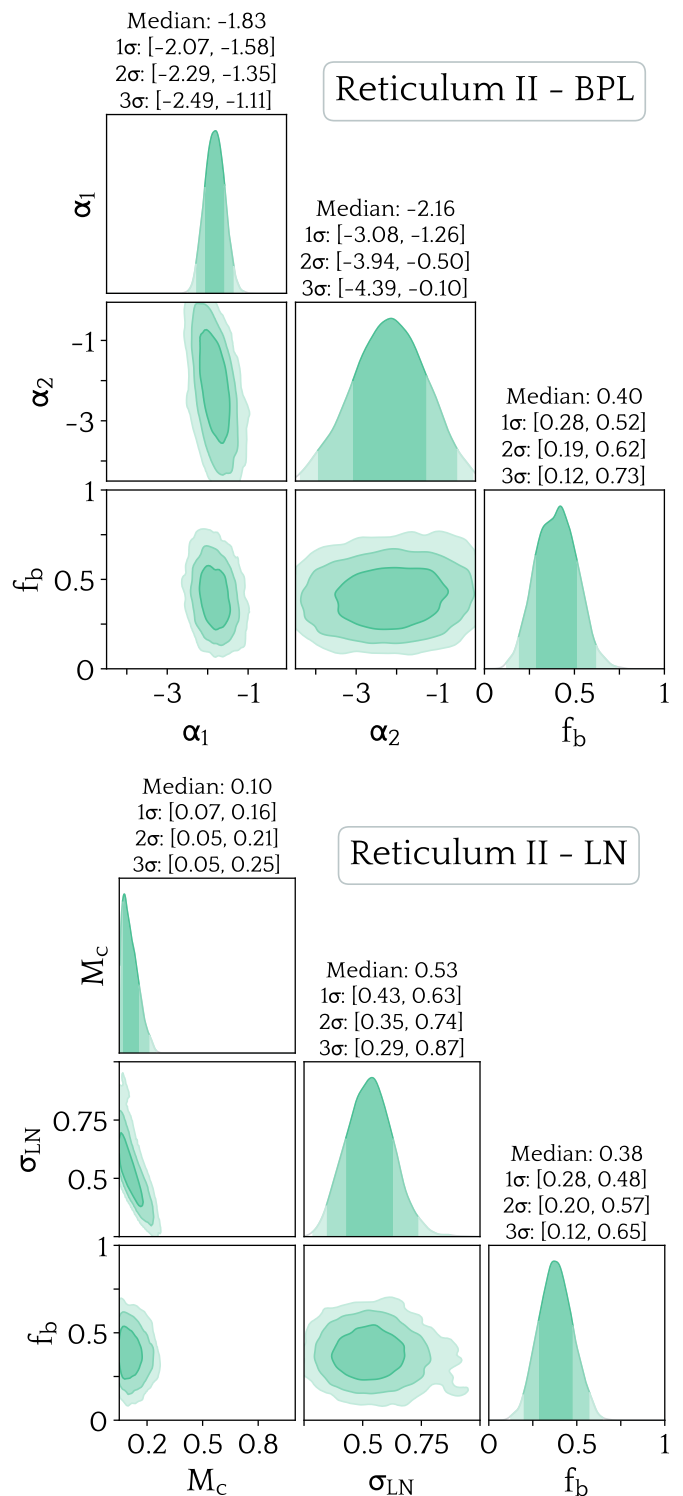


Fig. 4: Corner plots for the galaxy Reticulum II for two different initial mass functions: the broken power-law (upper panel) and log-normal (lower panel) distributions. The confidence levels, centred on the median, are represented by  $1\sigma$ ,  $2\sigma$ , and  $3\sigma$  intervals, with colours ranging from darker to lighter shades. The results are independent of  $f_{\text{PBH}}$  because of the low merit factor of Reticulum II.

in Segue 1 and Triangulum II. If PBH effects were sizeable, it would be difficult to explain the good agreement observed in the

inferred IMF parameters among these three galaxies. Hence, the possibility to derive constraints on the PBH fraction  $f_{\text{PBH}}$ . This suggests the following “control sample” strategy: one may use the posterior distributions of the IMF parameters and binary fraction inferred from Reticulum II as priors when analysing Segue 1 and Triangulum II.

Using these “control sample” priors for the three first parameters and uniform  $f_{\text{PBH}} \in [0, 3]$  – which allows PBHs to make up to 300% of the dark matter to conservatively avoid boundary effects on the tail of the posterior distribution – we performed the ABCSMC analysis from Sec. 4 for both Segue 1 and Triangulum II, and both parametrizations of the IMFs. The resulting posterior distributions are displayed in Appendix D. We show here in Fig. 5 only the marginalized distributions for our parameter of interest  $f_{\text{PBH}}$ .

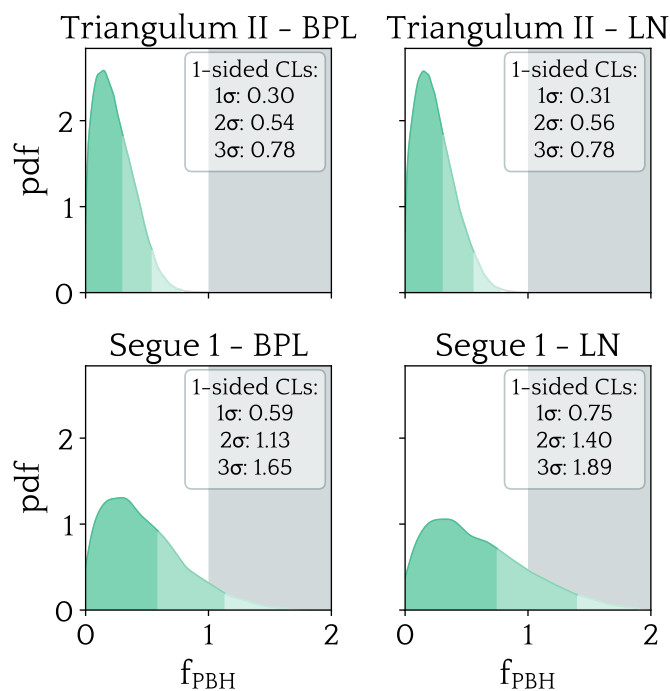


Fig. 5: Marginalized posterior probability density functions for the fraction of DM in PBHs,  $f_{\text{PBH}}$ , for the galaxies Triangulum II (upper panels) and Segue 1 (lower panels), adopting the broken power-law (left panels) and log-normal (right panels) initial mass functions. One-sided  $1\sigma$ ,  $2\sigma$  and  $3\sigma$  intervals are displayed with colours ranging from darker to lighter shades. The gray region corresponds to  $f_{\text{PBH}} > 1$ .

Using one-sided exclusion levels, one finds that for both forms of the stellar IMF, the galaxy Segue 1, for which the effect of PBHs is moderate, is not very constraining, as the value  $f_{\text{PBH}} = 1$  is excluded at the level of slightly less than  $2\sigma$ . In contrast, Triangulum II excludes PBHs as making more than  $\sim 55\%$  ( $\sim 78\%$ ) of the DM at a  $2\sigma$  ( $3\sigma$ ) confidence level. The value  $f_{\text{PBH}} = 1$  is excluded by Triangulum II at a  $3.7\sigma$  ( $4.1\sigma$ ) level for the BPL (LN) IMF. The results are overall quite similar for both IMFs, indicating that they are robust against the choice of the initial mass function law.

We also conducted the ABCSMC analysis using uniform priors for all parameters and found that  $f_{\text{PBH}} \gtrsim 1.2$  was excluded at the  $2\sigma$  level by Triangulum II in that case. This weaker exclusion can be attributed to the degeneracy between  $\alpha_1 / M_c$  and  $f_{\text{PBH}}$ . Uniform prior permits particularly high values of  $\alpha_1 \gtrsim -0.8$ ,

which are not commonly observed. Such a shallow slope in the BPL IMF would result in an overabundance of high-mass stars in the synthetic populations. Consequently, a high value of  $f_{\text{PBH}}$  would be required to destroy these excess high-mass stars and reproduce the observed present-day mass function. The same effect can be found for unrealistically high values of  $M_c \gtrsim 0.6$ , which also overproduces high-mass stars. Again, we emphasize that the uniform priors are less motivated than the “control sample” priors we used in our analysis, which exclude these unrealistically high values of  $\alpha_1$  and  $M_c$ .

Finally, we also performed an analysis using priors from a larger control sample. These new priors were obtained by combining the posterior distributions resulting from the analysis of Reticulum II and two other galaxies for which the data are available, and where the impact of PBHs is expected to be negligible, namely Ursa Major II and Boötes I. Although these galaxies are not as similar to our test galaxies as is Reticulum II, the priors obtained this way still exclude excessively high values of  $\alpha_1$  and  $M_c$ , which resulted in  $f_{\text{PBH}} = 1$  being excluded at more than  $3\sigma$  by Triangulum II. This demonstrates that our results are not solely due to using Reticulum II as a source of priors.

In Fig. 6, we present the constraints from Triangulum II (with the BPL mass function) on asteroid-mass primordial black holes around  $10^{19}$  g. We note again that, due to the uncertain effect of binary stars on PBH capture for masses above this range, it is not clear at the moment how to extend the constraints to higher masses. A more detailed study of binary systems may enable us to extend these constraints up to  $10^{21}$  g in the future.

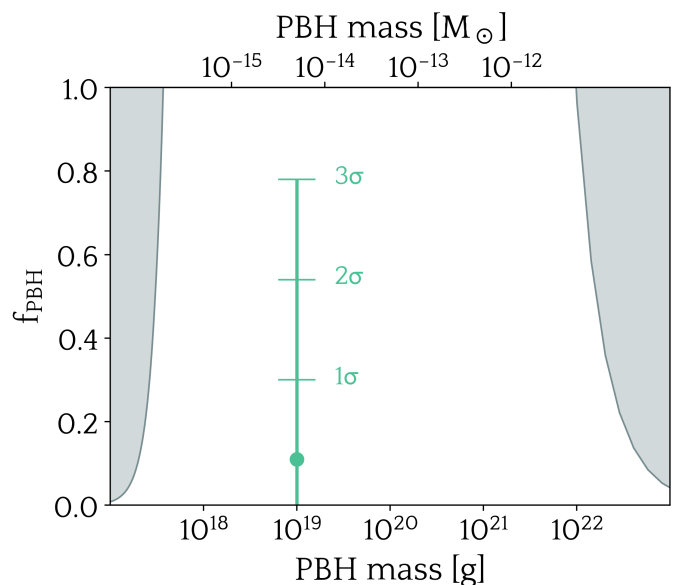


Fig. 6: Constraints on  $10^{19}$  g asteroid-mass primordial black holes from this work. The dot corresponds to the maximum of the posterior distribution of  $f_{\text{PBH}}$ , whose value is consistent with  $f_{\text{PBH}} = 0$ . To the left and the right, we show the existing constraints on PBHs arising from evaporation and microlensing, plotted using the data compiled in the PBH bounds repository (<https://github.com/bradkav/PBHbounds>).

## 6. Conclusion

In this work, we derived the first observationally based constraints in the previously open asteroid-mass window of primordial black

holes, hence showing that PBHs with masses around  $10^{19}$  g cannot constitute all the dark matter. We relied on the impact of these PBHs on the stellar mass function of ultra-faint dwarf galaxies and made use of photometric observations from the Hubble Space Telescope.

Assuming that the mean number of captured PBHs (Eq. 5) is unchanged for PBH masses  $\lesssim 10^{19}$  g, which is valid up to a  $\sim 30\%$  error (Esser & Tinyakov 2023; Tinyakov 2024), and using conservatively the bound derived in Appendix A for unperturbed PBHs in binary systems, the constraint from Sec. 5.2 can be extended to PBH masses between  $\sim 10^{18}$  and  $\sim 10^{20}$  g, as displayed in Fig. 7.

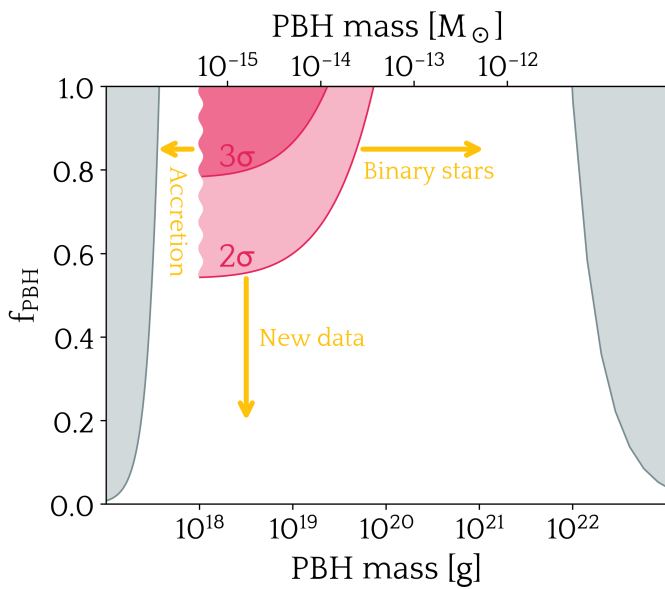


Fig. 7: Extended constraints on asteroid-mass primordial black holes between  $\sim 10^{18}$  and  $\sim 10^{20}$  g. The red-coloured regions correspond to the  $2\sigma$  (lighter) and  $3\sigma$  (darker) excluded values of  $f_{\text{PBH}}$ . The arrows indicate the directions in which the constraints may be improved in the future. To the left and the right, we show the existing constraints on PBHs arising from evaporation and microlensing.

While currently the constraints are marginal and cover a limited range of masses, future theoretical and observational advancements are expected to significantly improve these results, as indicated by the arrows in the figure.

In order to extend the constraints to lower masses, the accretion of stars by PBHs located in their cores must be studied more carefully. In Esser & Tinyakov (2023), the Bondi (1952) model was used to estimate the accretion time. It was found that the star destruction time scales inversely proportional to the PBH mass, approaching  $\sim 10$  Gyr for masses  $\lesssim 10^{18}$  g. In this mass range, factors of order 1 start to matter, so a more thorough analysis – one taking into account the radiation feedback within the accretion sphere and the rotation of the star – is required for a more accurate estimate of the destruction time. Some authors have already partially studied the subject, see, e.g., Markovic (1995).

To understand what happens for masses above  $\gtrsim 10^{19}$  g, the destruction probability of stars in binary systems by PBHs must be calculated. For now, we calculated in Appendix A the number of captured PBHs that are *unaffected* by the presence of a companion star, and conservatively assumed that all other PBHs are not captured. However, this is most likely not true, and

a dedicated three-body study of the binary star-PBH system is needed to understand the impact of binaries on the capture rate.

On the experimental side, there are multiple opportunities for advancement that may yield more stringent constraints in the near future. First, the PBH capture probability grows with decreasing velocity dispersion. New spectroscopic measurements of ultra-faint dwarf galaxies will improve our determination of their velocity dispersions, specifically for Triangulum II, where only an upper limit on  $\sigma_{\text{los}}$  exists at present. Using the actual value instead of the upper limit, as was done in this analysis, will definitely improve the constraints. Additionally, measuring velocity dispersions in other local dwarf galaxies may reveal new candidates where the PBH effect could be significant, or enlarge the number of galaxies which may be used as a “control sample”. Several large surveys, such as PFS (Takada et al. 2014) and DESI (Cooper et al. 2023), are expected to provide a substantial amount of new spectroscopic data in the coming years.

Another avenue for improvement lies in photometry: while the Hubble Space Telescope already enables very deep photometry, resolving stars with masses as low as  $\sim 0.2M_{\odot}$  in some dwarf galaxies, the James Webb Space Telescope can resolve even fainter stars (Weisz et al. 2023). This capability would increase the number of sources available for IMF analysis, yielding more precise determination of the latter and, consequently, more stringent constraints on the PBH fraction.

With increasingly numerous and precise spectroscopic and photometric measurements of dwarf galaxies, future studies will allow comparisons across galaxies with varying merit factors. This could facilitate investigations into possible correlations between the merit factor and the IMF parameters, thereby constraining PBHs by comparing a broad sample of galaxies rather than focusing on individual cases.

Another possibility for probing asteroid-mass PBHs could arise from their impact, through the star destruction process, on the chemical evolution of UFDs. Alternatively, direct observations of star destruction by PBHs may provide observable smoking-gun signatures (Markovic 1995; Bellinger et al. 2023; Caplan et al. 2024). However, much theoretical work is still needed in this direction to characterize the signal that may arise from such events.

## Acknowledgements

NE is a FRIA grantee of the Fonds de la Recherche Scientifique-FNRS and a member of BLU-ULB, the interfaculty research group focusing on space research at ULB - Université libre de Bruxelles. SDR is co-funded by the European Union (MSCA EDUCADO, GA 101119830). Views and opinions expressed are however those of the author(s) only and do not necessarily reflect those of the European Union. Neither the European Union nor the granting authority can be held responsible for them. The HST data were observed as part of Treasury Program GO-14734 (PI Kallivayalil). Support for this program was provided by NASA through grants from the Space Telescope Science Institute, which is operated by the Association of Universities for Research in Astronomy, Incorporated, under NASA contract NAS5-26555. PT is supported in part by the Institut Interuniversitaire des Sciences Nucléaires (IISN) Grant No. 4.4503.15. RFGW is grateful for support through the generosity of Eric and Wendy Schmidt, by recommendation of the Schmidt Futures program. Computational resources have been provided by the Consortium des Equipements de Calcul Intensif (CECI), funded by the Fonds de la Recherche Scientifique de Belgique (F.R.S.-FNRS) under



Grant No. 2.5020.11 and by the Walloon Region. Tag: ULB-TH/25-01.

## References

- Bastian, N., Covey, K. R., & Meyer, M. R. 2010, *ARA&A*, 48, 339
- Bellinger, E. P., Caplan, M. E., Ryu, T., et al. 2023, *Astrophys. J.*, 959, 113
- Belokurov, V., Zucker, D. B., Evans, N. W., et al. 2007, *ApJ*, 654, 897
- Bondi, H. 1952, *Monthly Notices of the Royal Astronomical Society*, 112, 195
- Capela, F., Pshirkov, M., & Tinyakov, P. 2013, *Phys. Rev. D*, 87, 023507
- Capela, F., Pshirkov, M., & Tinyakov, P. 2014, *Phys. Rev. D*, 90, 083507
- Caplan, M. E., Bellinger, E. P., & Santarelli, A. D. 2024, *Astrophys. Space Sci.*, 369, 8
- Carr, B., Kohri, K., Sendouda, Y., & Yokoyama, J. 2021, *Reports on Progress in Physics*, 84, 116902
- Chabrier, G. 2003, *Proceedings of the Astronomical Society of the Pacific*, 115, 763
- Cooper, A. P., Kuposov, S. E., Allende Prieto, C., et al. 2023, *ApJ*, 947, 37
- Dotter, A., Chaboyer, B., Jevremović, D., et al. 2008, *Astrophysical Journal Supplement Series*, 178, 89
- El-Badry, K., Weisz, D. R., & Quataert, E. 2017, *MNRAS*, 468, 319
- Esser, N., De Rijcke, S., & Tinyakov, P. 2024, *Mon. Not. Roy. Astron. Soc.*, 529, 32
- Esser, N. & Tinyakov, P. 2023, *Phys. Rev. D*, 107, 103052
- Filion, C., Platais, I., Wyse, R. F. G., & Kozhurina-Platais, V. 2022, *ApJ*, 939, 38
- Filion, C., Wyse, R. F. G., Richstein, H., et al. 2024, *The Astrophysical Journal*, 967, 165
- Geha, M., Brown, T. M., Tumlinson, J., et al. 2013, *ApJ*, 771, 29
- Gennaro, M., Tchernyshyov, K., Brown, T. M., et al. 2018, *The Astrophysical Journal*, 855, 20
- Hawking, S. 1971, *Monthly Notices of the Royal Astronomical Society*, 152, 75
- Ji, A. P., Frebel, A., Chiti, A., & Simon, J. D. 2016, *Nature*, 531, 610
- Kirby, E. N., Cohen, J. G., Simon, J. D., et al. 2017, *ApJ*, 838, 83
- Kroupa, P. 2001, *Monthly Notices of the Royal Astronomical Society*, 322, 231
- Markovic, D. 1995, *MNRAS*, 277, 25
- Moe, M., Kratter, K. M., & Badenes, C. 2019, *ApJ*, 875, 61
- Muñoz, R. R., Côté, P., Santana, F. A., et al. 2018, *ApJ*, 860, 66
- Navarro, J. F., Frenk, C. S., & White, S. D. M. 1997, *ApJ*, 490, 493
- Oncins, M., Miralda-Escudé, J., Gutiérrez, J. L., & Gil-Pons, P. 2022, *Mon. Not. Roy. Astron. Soc.*, 517, 28
- Patel, E., Kallivayalil, N., Garavito-Camargo, N., et al. 2020, *The Astrophysical Journal*, 893, 121
- Plummer, H. C. 1911, *Mon. Not. Roy. Astron. Soc.*, 71, 460
- Raghavan, D., McAlister, H. A., Henry, T. J., et al. 2010, *Astrophysical Journal Supplement Series*, 190, 1
- Richstein, H., Kallivayalil, N., Simon, J. D., et al. 2024, *ApJ*, 967, 72
- Sacchi, E., Richstein, H., Kallivayalil, N., et al. 2021, *The Astrophysical Journal Letters*, 920, L19
- Schälte, Y., Klinger, E., Alamoudi, E., & Hasenauer, J. 2022, *Journal of Open Source Software*, 7, 4304
- Simon, J. D. 2019, *Annual Review of Astronomy and Astrophysics*, 57, 375–415
- Simon, J. D., Brown, T. M., Mutlu-Pakdil, B., et al. 2023, *The Astrophysical Journal*, 944, 43
- Simon, J. D., Drlica-Wagner, A., Li, T. S., et al. 2015, *The Astrophysical Journal*, 808, 95
- Simon, J. D., Geha, M., Minor, Q. E., et al. 2011, *ApJ*, 733, 46
- Takada, M., Ellis, R. S., Chiba, M., et al. 2014, *PASJ*, 66, R1
- Tinyakov, P. 2024, *arXiv [arXiv:2406.03114]*
- Weisz, D. R., McQuinn, K. B. W., Savino, A., et al. 2023, *ApJS*, 268, 15
- Wolf, J., Martinez, G. D., Bullock, J. S., et al. 2010, *Monthly Notices of the Royal Astronomical Society*, 406, 1220
- Wyse, R. F. G., Moe, M., & Kratter, K. M. 2020, *MNRAS*, 493, 6109
- Zel'dovich, Y. B. & Novikov, I. D. 1967, *Soviet Astronomy*, 10, 602

## Appendix A: PBHs and binary stars

### Appendix A.1: Analytical expression of $\nu$ for single stars

As was shown by numerical simulations in Esser & Tinyakov (2023) and analytically in Oncins et al. (2022), the number of primordial black holes orbiting around a newly formed star with Keplerian periastron  $r_{\min}$  and apastron  $r_{\max}$  is given by (Tinyakov 2024)

$$\frac{d\nu}{dr_{\min}dr_{\max}} = \frac{f_{\text{PBH}}\rho_{\text{DM}}}{m(\sqrt{2}\sigma_v)^3} (3\pi R_g)^{3/2} \frac{1}{\sqrt{2}r_{\max}} \quad (\text{A.1})$$

with  $m$  the PBH mass,  $\sigma_v$  the velocity dispersion assumed to be the same as for stars, and  $R_g = 2GM$  the Schwarzschild radius of the star.

In the absence of close external perturbers such as a binary companion, the PBHs that will end up captured by the star are the ones which (i) have star-crossing orbits, i.e.  $r_{\min} < R$ , and (ii) lose enough energy due to the dynamical friction during each encounter with the star, so that their orbits become fully enclosed inside the latter in a time of order the age of stars in UFDs. This second condition can be expressed, assuming the star is uniform in density, as (Esser & Tinyakov 2023)

$$r_{\max} < r_T = \left( \frac{Tm \ln \Lambda}{\pi MR} \right)^2 R_g \simeq 142 \left( \frac{m}{10^{20}\text{g}} \right)^2 \text{AU}, \quad (\text{A.2})$$

where  $T = 13$  Gyr is the time since star formation,  $\ln \Lambda \simeq 30$  is the Coulomb logarithm and the numerical value on the right-hand side assumes  $M = M_\odot$  and  $R = R_\odot$ .

Integrating Eq. (A.1) over  $r_{\min}$  and  $r_{\max}$  with the conditions (i) and (ii), one finds the mean number  $\nu_{\text{single}}$  of PBHs that are captured by a single star in the absence of perturbers<sup>5</sup>. One can see by combining Eqs. (A.1) and (A.2) that this number is independent of the PBH mass: while lighter black holes are more numerous at fixed  $\rho_{\text{DM}}$ , they experience less dynamical friction when colliding with the star and thus only the ones that start with smaller orbits end up captured. This also justifies why the survival probability formula (6) is valid in the range  $m \in [10^{19}, 10^{21}]$ g without depending on the PBH mass.

### Appendix A.2: Conservative bound on $\nu$ for binary stars

When a nearby perturber, such as a companion star, is present, a conservative condition for the PBH to be captured is that the angular momentum imparted to the PBH by the perturber remains sufficiently small, ensuring the PBH's periastron stays within the primary star's radius during two successive crossings. Assuming that the perturber is static over this time and located at a distance  $D \gg r_{\max}$  from the primary star, this condition can be written (Esser & Tinyakov 2023)

$$r_{\max} < r_D = (\alpha R D^6)^{1/7}, \quad (\text{A.3})$$

where  $\alpha$  is a  $\mathcal{O}(1)$  calculable numerical coefficient depending on the direction of the perturber.

Extrapolating this formula to be valid for values of  $D$  as small as  $r_{\max}$ , and assuming conservatively that PBHs are not captured when  $D < r_{\max}$ , one can obtain a lower bound on the number of PBHs that are captured by the primary star in the

<sup>5</sup>  $\nu_{\text{single}}$  is the analytical equivalent of Eq. (5), except that it does not take into account the non-uniform density profile of the primary star, and the possible deviation of PBHs by distant (other than companion stars) perturbers.

presence of a companion by integrating Eq. (A.1) for (i)  $r_{\min} < R$  and (ii)  $r_{\max} < r_C = \min(r_T, r_D, D)$ . Of course, the result will depend on the distance  $D$  to the companion. Assuming that it is distributed according to some function  $f(D)$  among the stellar binaries population, the conservative bound can then be obtained as

$$\nu_{\text{binary}} = \int_0^R \int_0^\infty \int_{r_{\min}}^{r_C} \frac{d\nu}{dr_{\min}dr_{\max}} f(D) dr_{\max} dD dr_{\min}. \quad (\text{A.4})$$

We infer the distribution  $f(D)$  from measurements of binary orbital periods  $P$  of nearby sun-like stars, with spectral types ranging from F6 to K3, by Raghavan et al. (2010), who find a log-normal period distribution with  $\log_{10}(P/\text{day}) = 5.03$  and  $\sigma_{\log_{10}(P/\text{day})} = 2.28$ . Using Kepler's third law for circular orbits, the distribution of periods can be converted into the distribution of distances  $D$ , which also follows a log-normal distribution  $f(D)$ . While it is known that the close-binary fraction is higher for metal-poor solar-type stars, such as those in UFDs (Moe et al. 2019; Wyse et al. 2020), in the absence of a measured orbital period distribution we simply adopt the results for local (primarily solar metallicity) binary systems.

Assuming sun-like primary and companion stars, we computed the ratio  $\nu_{\text{binary}}/\nu_{\text{single}}$  for various PBH masses<sup>6</sup>. It is displayed on Fig. A.1. We checked that this result changed only slightly with the stellar masses and the primary star's radius.

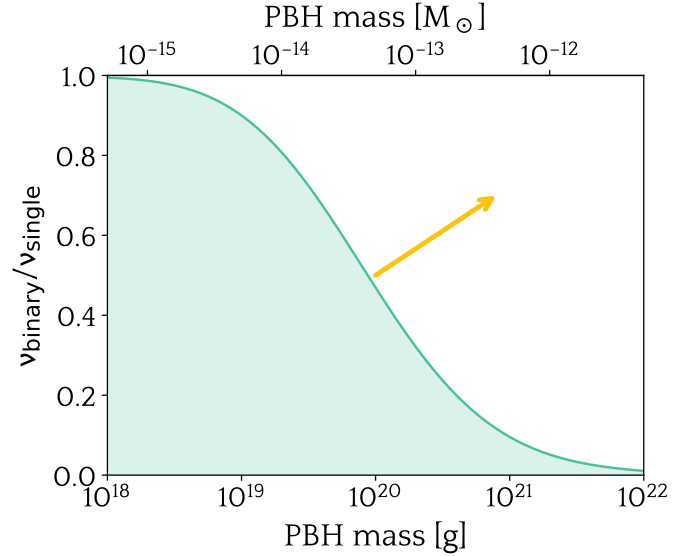


Fig. A.1: Ratio of the mean number of PBHs captured by stars in binary systems to the mean number captured by single stars, under the very conservative assumptions described in the text. While the coloured region represents a conservative estimate that cannot be reduced further, the arrow indicates that a more thorough analysis could potentially expand this region.

One can see that lighter PBHs are less affected by the presence of binaries, because the condition that they lose their energy sufficiently quickly (Eq. (A.2)) implies that only the light PBHs with very small orbits, usually significantly smaller than the distance between the primary star and its companion, end up captured. For heavier PBHs, larger orbits are allowed, but these orbits are

<sup>6</sup> With Eq. (A.1) and a log-normal distribution for  $f(D)$ , Eq. (A.4) can be computed analytically in terms of Erf and Erfc functions.

then perturbed and the PBHs may not end up being captured. However, we emphasize here that this result is a conservative *lower bound* on the number of captured PBHs in binaries. To know what happens for large PBH masses, one would need to perform a full 3-body study.

We conclude from this calculation that most PBHs with masses  $\lesssim 10^{19}$ g are not affected by binary companions. Hence, we can safely use the expression (5) for  $\nu(M)$  up to this mass. Above this value, what happens remains unclear and will need to be studied in the future. Note however that at a mass of  $\sim 10^{20}$ g, a sizeable fraction of  $\sim 50\%$  of PBHs is still unaffected by companion stars.

## Appendix B: CMDs for Triangulum II and Segue 1

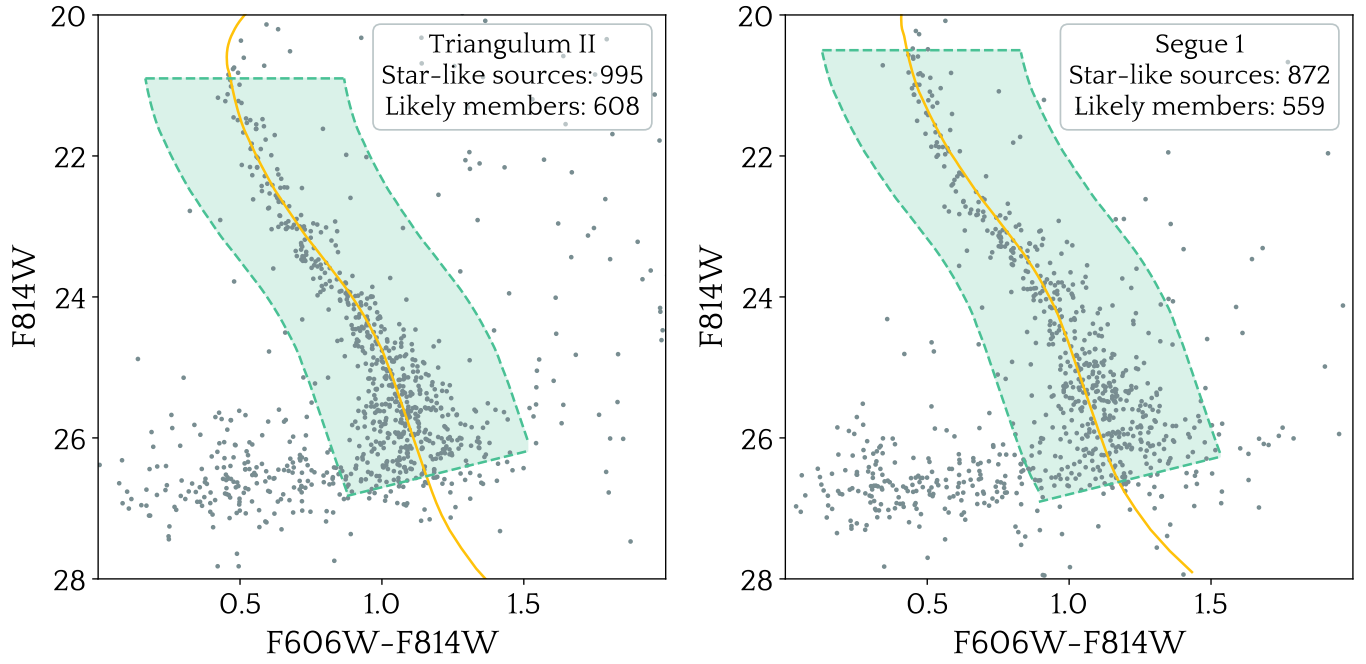


Fig. B.1: Colour-magnitude diagrams of Triangulum II (left panel) and Segue 1 (right panel). The solid lines represent the Dartmouth isochrone for a population of 13 Gyr old stars with metallicity  $[Fe/H] = -2.5$ , corrected for distance and extinction. The points correspond to the observed star-like sources, while the coloured regions encompass the stars that are likely members of the galaxies and that will be used to study their stellar mass functions.



## Appendix C: Corner plots for Triangulum II and Segue 1 – no PBHs

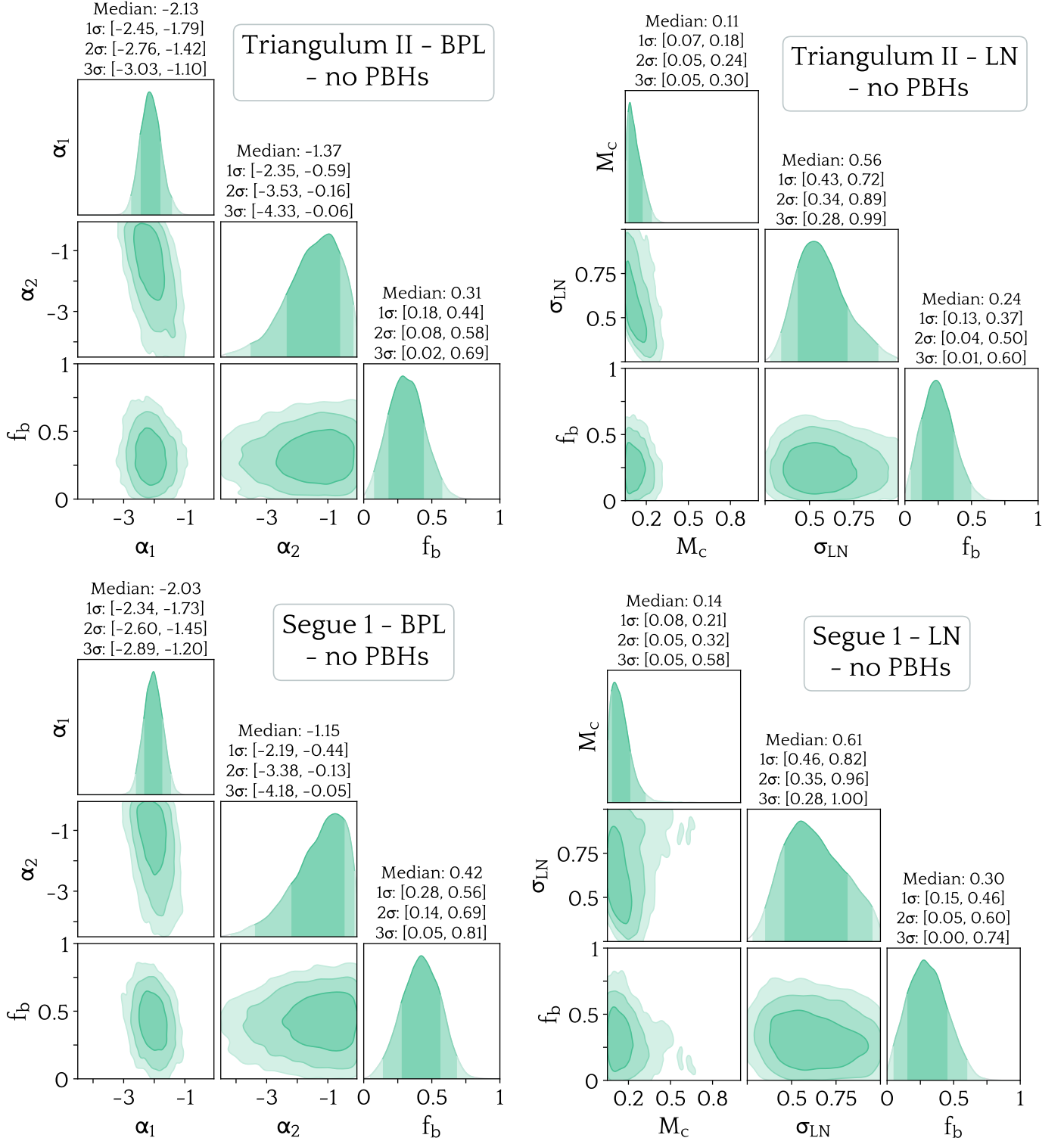


Fig. C.1: Corner plots for the galaxies Triangulum II (upper panels) and Segue 1 (lower panels), with no PBH effect ( $f_{PBH} = 0$ ) and for two different initial mass functions: the broken power-law (left panels) and log-normal (right panels) distributions. The confidence levels, centred on the median, are represented by 1 $\sigma$ , 2 $\sigma$ , and 3 $\sigma$  intervals, with colours ranging from darker to lighter shades.

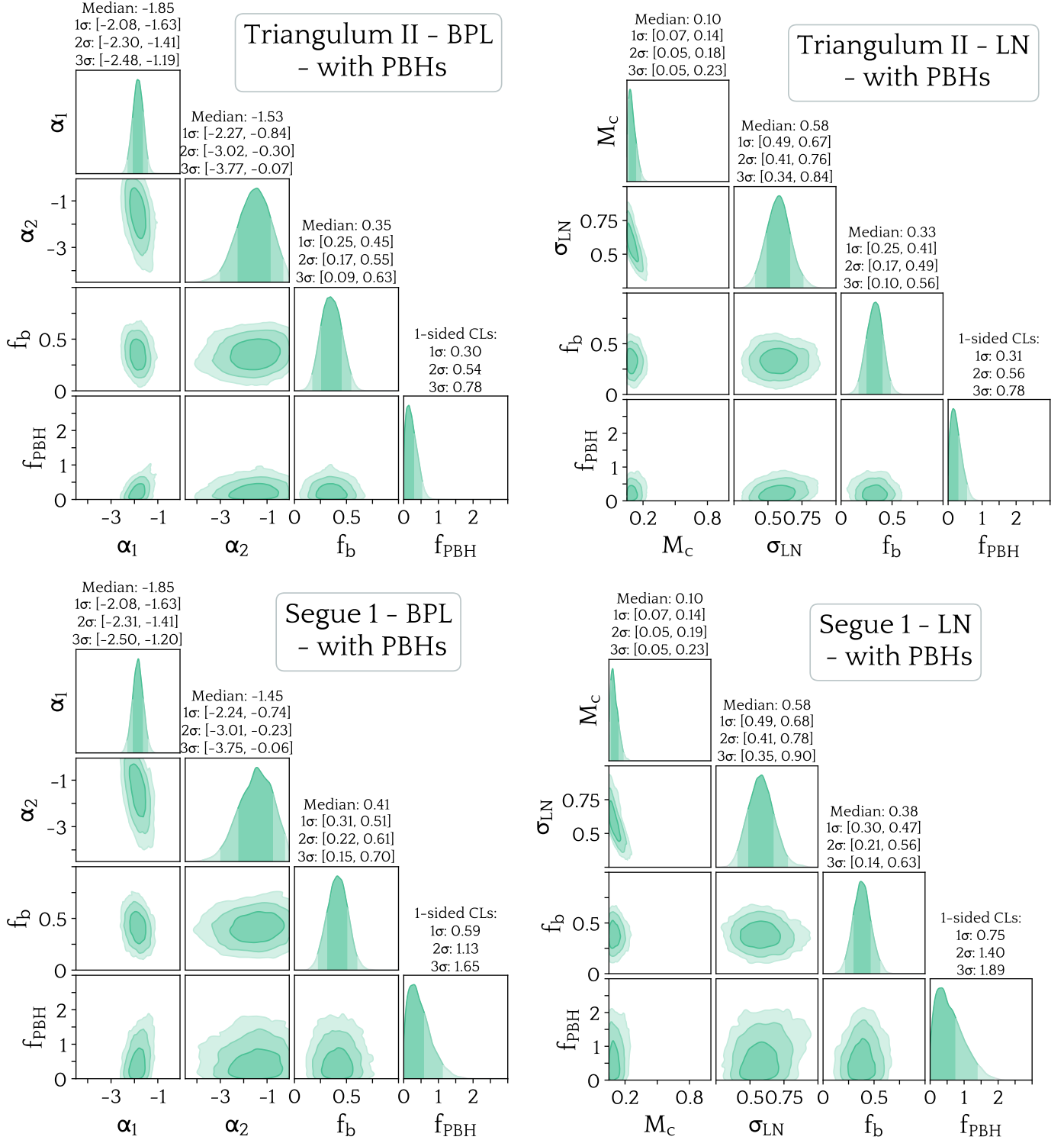
**Appendix D: Corner plots for Triangulum II and Segue 1 – with PBHs**


Fig. D.1: Corner plots for the galaxies Triangulum II (upper panels) and Segue 1 (lower panels), with PBH effect and for two different forms of the stellar initial mass function: the broken power-law (left panels) and log-normal (right panels) distributions. The confidence levels for all parameters are centred on the median, except for  $f_{\text{PBH}}$  where the levels are one-sided. They are represented by 1 $\sigma$ , 2 $\sigma$ , and 3 $\sigma$  intervals, with colours ranging from darker to lighter shades.